Article

Not peer-reviewed version

Tuning Oxygen Reduction Kinetics in LaSrCoO4 with Strained Epitaxial Thin Films and Wrinkled Freestanding Membranes

Habib Rostaghi Chalaki , Ebenezer Seesi , Mohammad El Loubani , Dongkyu Lee *

Posted Date: 15 December 2025

doi: 10.20944/preprints202512.1332.v1

Keywords: epitaxial thin films; freestanding oxide membranes; oxygen reduction reaction; pulsed laser deposition; ruddlesden-popper oxides

Preprints.org (www.preprints.org) | NOT PEER-REVIEWED | Posted: 15 December 2025 doi:10.20944/preprints202512.1332.v1

Article

Tuning Oxygen Reduction Kinetics in $LaSrCoO_4$ with Strained Epitaxial Thin Films and Wrinkled Freestanding Membranes

Habib Rostaghi Chalaki, Ebenezer Seesi, Mohammad El Loubani and Dongkyu Lee *

Department of Mechanical Engineering, College of Engineering and Computing, University of South Carolina, Columbia, SC 29208, USA

* Correspondence: dongkyu@cec.sc.edu

Abstract

Sluggish oxygen reduction reaction (ORR) remains a critical barrier to advancing intermediate-temperature electrochemical energy devices. Here, we demonstrate that strain engineering in two platforms, epitaxial thin films and freestanding membranes, systematically tunes ORR kinetics in Ruddlesden-Popper $LaSrCoO_4$. In epitaxial films, the thickness is varied to control in-plane tensile strain, whereas in freestanding membranes strain relaxation during the release step of fabrication with water soluble sacrificial layers produces flat or wrinkled architectures. Electrochemical impedance spectroscopy analysis reveals more than an order of magnitude increase in the oxygen surface exchange coefficient for tensile-strained films relative to relaxed films, together with a larger oxygen vacancy concentration. Wrinkled freestanding membranes provide a further increase in oxygen surface exchange kinetics and a lower activation energy, which are attributed to increased active surface area and local strain variation. These results identify epitaxial tensile strain and controlled wrinkling as practical design parameters for optimizing ORR activity in Ruddlesden-Popper oxides.

Keywords: epitaxial thin films; freestanding oxide membranes; oxygen reduction reaction; pulsed laser deposition; ruddlesden-popper oxides

1. Introduction

Developing intermediate-temperature solid oxide fuel cells (IT-SOFCs), which are promising electrochemical devices for environmentally friendly, efficient energy production and conversion, requires overcoming sluggish cathodic oxygen reduction reaction (ORR) at intermediate temperatures [1–7]. Mixed ionic and electronic conducting ABO_3 perovskites, such as $La_{1-x}Sr_xCo_{1-y}Fe_yO_{3-\delta}$ (LSCF113) and $La_{1-x}Sr_xCoO_{3-\delta}$ (LSC113) are widely used as electrodes because concurrent electronic conduction and mobile oxygen vacancies extend the electrochemically active region from the triple-phase boundary to the entire electrode surface [8–13]. However, these ABO_3 perovskites suffer from high thermal expansion coefficients and low chemical stability due to facile lattice oxygen loss, which causes undesirable lattice expansion in reducing atmospheres [14,15]. In addition, surface Sr segregation, a primary degradation pathway in LSCF113 and LSC113, suppresses ORR kinetics over time [11,16–18].

Ruddlesden–Popper (RP) oxides are attractive alternatives since they offer good electronic conductivity together with good thermal and chemical stability [19–22]. RP structures consist of n consecutive perovskite layers (ABO_3) alternating with rock-salt layers (AO) along the crystallographic *c*-axis direction [23,24]. Within this family, oxygen-vacancy-dominated $La_{2-x}Sr_xCoO_{4\pm\delta}$ is notable for stable reduction behaviors over a wide range of temperatures (300 ~ 1500 °C) [25–27] and oxygen surface exchange kinetics comparable to those of LSCF113 and LSC113 [28,29]. Moreover, when $La_{2-x}Sr_xCoO_4$ is interfaced with perovskites such as LSCF113 or LSC113, the heterostructured interface can yield fast oxygen surface exchange [30,31]. Nevertheless, for stand-alone $La_{2-x}Sr_xCoO_{4\pm\delta}$ the intrinsic ORR activity at intermediate temperatures still requires further improvement for IT-SOFCs.

Epitaxial oxide thin films have shown remarkable enhancements in ORR kinetics by enabling controlled structure–property tuning not accessible in bulk [8,32]. In such films, epitaxial strain is a key design parameter that modifies oxygen vacancy formation energies and surface chemistry, thereby controlling both bulk oxygen transport and oxygen surface exchange kinetics [32–35]. For ABO_3 perovskites, tensile strain, introduced via substrate choice or reduced film thickness, is widely reported to enhance oxygen surface exchange kinetics [36,37]. By contrast, only a few studies have investigated strain effects in RP oxides, and the reported influence of epitaxial strain on ORR activity is inconsistent, with both enhancement and suppression observed [19,21,38–40]. Consequently, the strain dependence of oxygen surface exchange kinetics in RP oxides remains unresolved.

Beyond epitaxial strain, epitaxial oxide films provide a platform to create freestanding oxide membranes, enabling morphological control beyond substrate clamping [41]. Freestanding membranes fabricated by wet etching maintain high crystallinity and structural quality [42–45]. During dissolution of the sacrificial layer, strain relaxation can leave the membrane flat or produce wrinkled architectures [41]. Wrinkling introduces spatially varying local strain and curvature, and can increase the density of active ORR sites. Such wrinkled geometries have been used to enhance functional properties, including piezoelectric and optoelectronic properties, in other oxide systems [46–48]. However, the direct impact of controlled wrinkling on ORR kinetics in MIEC oxides has, to our knowledge, not been investigated, leaving a clear opportunity to couple increased surface area and local strain for catalytic benefit.

In this study, we use $LaSrCoO_4$ (LSC214) as a model RP oxide to investigate two design parameters, epitaxial strain and membrane wrinkling, for accelerating ORR at intermediate temperatures. First, we grow epitaxial LSC214 films on (001) single-crystal yttria-stabilized zirconia (YSZ) and systematically vary thickness to tune in-plane tensile strain. YSZ provides high oxide-ion conductivity with negligible electronic leakage while serving as a single-crystal growth platform, which in practice makes thickness-controlled strain the most general approach for films on YSZ [9,33,49]. Second, we fabricate freestanding LSC214 membranes via wet etching to induce controlled wrinkling, enabling simultaneous manipulation of active surface area and local strain fields in the absence of substrate clamping. Taken together, our results establish epitaxial strain and wrinkling as design strategies for optimizing ORR activity in RP oxides and provide practical design rules for next-generation IT-SOFC cathodes.

2. Materials and Methods

2.1. Synthesis of Epitaxial Thin Films

Epitaxial LSC214 thin films with four different thicknesses were grown on (001) single-crystal YSZ substrates using pulsed laser deposition (PLD). Prior to the LSC214 growth, a ~5 nm $Gd_{0.2}Ce_{0.8}O_2$ (GDC) buffer layer was deposited to prevent the formation of a $La_2Zr_2O_7$ layer at the interface [50]. The platinum ink (Pt) counter electrode (#6082, ASF, USA) was applied to the back side of the YSZ substrate and dried in air at 900 °C for 1 hour before the deposition of LSC214 and GDC layers. To ensure thermal contact, a small amount of silver paint (Leitsilber 200, Ted Pella, USA) was used to affix the YSZ substrate to the PLD substrate holder.

PLD was carried out using a KrF excimer laser with a wavelength (λ) of 248 nm, a pulse rate of 10 Hz, and a pulse energy of 45 mJ under an oxygen partial pressure (pO_2) of 6.6×10^{-5} atm (50 mTorr). The GDC buffer (~5 nm; 500 pulses) was deposited at 550 °C, followed by 1000, 2000, 5000, and 10000 pulses of LSC214 at 650 °C, resulting in film thicknesses of ~20, 37, 69, and 129 nm, respectively. Film thickness was determined from atomic force microscopy (AFM) step-height measurements across a masked edge. After LSC214 growth, samples were cooled to room temperature in the PLD chamber for ~1 hour under a pO_2 of 6.6×10^{-5} atm (50 mTorr).

2.2. Synthesis of Freestanding Membranes

Freestanding LSC214 membranes were fabricated by depositing LSC214 on water-soluble sacrificial layers, $Sr_2CaAl_2O_6$ (S_2C_1AO) and $SrCa_2Al_2O_6$ (S_1C_2AO), grown on (001) single-crystal $SrTiO_3$ (STO) substrates by PLD. A ~5 nm GDC buffer layer was inserted between LSC214 and the sacrificial layers to improve lattice coherence and prevent interdiffusion. S_2C_1AO was deposited under vacuum, whereas S_1C_2AO was deposited at a pO_2 of 1.31×10^{-4} atm (100 mTorr). The PLD conditions were 1500 pulses for the 30 nm sacrificial layer at 750 °C, 500 pulses for the GDC buffer at 550 °C, followed by 8000 pulses of LSC214 at 650 °C, resulting in a total LSC214 film thickness of about 120 nm.

A 100 μm-thick polypropylene carbonate (PPC) layer was spin-coated on LSC214 to serve as mechanical support. The PPC/LSC214/GDC/S_2C_1AO or S_1C_2AO/STO stack was then immersed in deionized water to dissolve the sacrificial layer, releasing the freestanding PPC/LSC214/GDC membrane from the STO substrate. The detached membrane was transferred onto a YSZ substrate pre-coated with a Pt counter electrode, after which the PPC support layer was removed using chloroform etching to yield a pristine freestanding LSC214 membrane for electrochemical measurements.

2.3. Thin Film and Freestanding Membrane Characteristics

High-resolution X-ray diffraction (HRXRD) was performed using a four-circle diffractometer to examine the phase purity and crystal orientation of the thin film systems. Measurements were conducted in both in-plane and out-of-plane configurations. YSZ has a cubic structure (lattice parameter $a = b = c$) [51], and thus the lattice parameter, a, was directly determined from the YSZ (202) reflection. LSC214 has tetragonal symmetry with space group I4/mmm [52], where the c-axis lattice parameter was determined from the LSC214 (002) reflection, and assuming a- and b-axis lattice parameters are equivalent, the in-plane lattice parameter was determined from the LSC214 (103) reflection. $\hat{a}$ and $\hat{c}$, which are the relaxed lattice parameters for films in an unstrained state, were obtained from the following equation [10,49,53],

$$\frac{(c-\hat{c})}{\hat{c}}=\frac{-2\nu}{1-\nu}\frac{(a-\hat{a})}{\hat{a}}, \tag{1}$$

assuming $\hat{c}/\hat{a} = 3.285$ at 298K [52] and $\nu = 0.3$ [10,49,53,54].

In-plane and out-of-plane strains were calculated from the following equations. The in-plane strain is given by ε_{aa}, and the out-of-plane strain by ε_{cc}.

$$\varepsilon_{aa}=\frac{(a-\hat{a})}{\hat{a}}\ ,\ \varepsilon_{cc}=\frac{(c-\hat{c})}{\hat{c}}. \tag{2}$$

Surface morphology of the freestanding membranes was examined using optical microscopy (Carl Zeiss, Germany).

2.4. Oxygen Surface Exchange Kinetics

In-situ electrochemical impedance spectroscopy (EIS) was performed at open circuit with a microprobe station (Karl Süss, Germany) connected to a frequency response analyzer (Solartron 1260, USA) and dielectric interface (Solartron 1296, USA). For epitaxial films, circular microelectrodes of ~200 μm diameter were used. For freestanding membranes, 5 × 5 mm² LSC214 squares with a central Ag contact dot (~200 μm diameter) were prepared. The temperature was controlled at 550 °C on a heating stage (Linkam TS1500, UK) and verified by a thermocouple in contact with the film surface (±5 °C variation). Impedance spectra were collected with 10 mV amplitude from 1 MHz to 1 mHz over pO_2 spanning from 10^{-3} to 1 atm using calibrated O_2/N_2 mixtures. ZView software (Scribner Associates, USA) was used to construct an equivalent circuit and perform complex least squares fitting. An equivalent circuit, $R_1(R_2CPE_2)(R_{ORR}CPE_{ORR})$, was used to analyze the EIS data, where R_1 is the ohmic resistance, R_2/CPE_2 represent the middle frequency process, and R_{ORR}/CPE_{ORR} represent the low frequency ORR process. This model was used to extract the ORR resistance and the oxygen surface exchange coefficient. The electrical surface exchange coefficient (k^q), which is comparable to k^* [55], was calculated as [56,57],

$$k^q = RT/4F^2 R_{ORR} A_{electrode} c_o, \tag{3}$$

where R is the universal gas constant (8.314 J.mol^{-1}.K^{-1}), T is the absolute temperature, F is Faraday's constant (96,500 C.mol^{-1}), R_{ORR} is the resistance from the low frequency feature, $A_{electrode}$ is the electrode area, and c_o is the lattice oxygen concentration in LSC214, with

$$c_o = (4+\delta)/V_m, \tag{4}$$

where V_m is the molar volume of LSC214 at room temperature. In this study, c_o was calculated with δ extracted from previously reported values [58].

The volume specific capacitance (*VSC*), indicative of changes in δ induced by changes in the electrical potential, was obtained from EIS data via the expression,

$$VSC = [1/(A_{electrode} \times t)]((R_{ORR})^{1-n}Q)^{1/n}, \tag{5}$$

where t is the electrode thickness, Q is the non-ideal "capacitance", and n is the non-ideality factor of constant phase element (CPE). The fitted n values for semi-circle CPE_{ORR} were found to range from ~ 0.96 to 1.0 over the entire pO_2 range examined (n =1, ideal).

2.5. Surface Analysis of Thin Films

Surface chemistry of the LSC214 films before and after heat treatment was analyzed using ex-situ auger electron spectroscopy (AES) with the Physical Electronics 700 Scanning Auger Nanoprobe (PHI, USA). The AES measurements were performed at an accelerating voltage of 10 kV. To investigate the effects of heat treatment, the LSC214 films were annealed at 550 °C for 6 hours under two different pO_2 of 10^{-3} and 1 atm. For AES data collection, three randomly selected spots with dimensions of 10 μm × 10 μm were chosen on each sample within an ultra-high vacuum chamber.

3. Results

3.1. Crystallinity and Strain of the LSC214 Thin Films and Freestanding Membranes

Figure 1 shows the HRXRD data of the epitaxial LSC214 films. The out-of-plane XRD pattern revealed the presence of $(00l)_{tetragonal}$ peaks of LSC214 (where *l* is even) and $(00l)_{cubic}$ peaks of GDC and YSZ, indicating the successful synthesis of *c*-axis-oriented epitaxial LSC214 films with a crystallographic relationship of $(002)_{tetragonal}$ LSC214 // $(002)_{cubic}$ GDC // $(002)_{cubic}$ YSZ (Figure 1a). The ϕ scans of the LSC214 films confirmed that LSC214 $(103)_{tetragonal}$, GDC $(202)_{cubic}$, and YSZ $(202)_{cubic}$ have strong peaks with four-fold cubic symmetry (Figure 1b), which reveals the in-plane crystallographic relationships between GDC and YSZ (cube-on-cube alignment) and LSC214 and GDC (in-plane 45° rotation) as shown in Figure 1c. The measured lattice parameters *a* and *c* of the LSC214 films were found to be a = 3.806 Å and c = 12.51 Å for 129 nm at RT, in good agreement with literature data (a = 3.807 Å and c = 12.507 Å for the *c*-axis oriented epitaxial LSC214 thin film with ~100 nm) [59]. Note that perovskite oxides often reveal a gradual strain relaxation as the film thickness is increased, which is most likely due to the formation of complex defect structures (such as dislocations) at the film/substrate interface to relieve the built-up elastic energy resulting from the strain. Such a phenomenon is also observed in this work, providing more than one strain state through the use of multiple film thicknesses. At room temperature, the 20, 37, and 69 nm films were tensile strained with the strain magnitude decreasing as the film thickness increased. However, the 129-nm-thick film was fully relaxed. These strains arise due to significant variations in atomic spacing between LSC214 and GDC in the (001) LSC214 orientation. Table 1 shows the relaxed lattice parameters ($\hat{a}$ and $\hat{c}$) of LSC214 films, ranging from 3.807 to 3.811 Å and from 12.503 to 12.515 Å, respectively.

Preprints.org (www.preprints.org) | NOT PEER-REVIEWED | Posted: 15 December 2025 doi:10.20944/preprints202512.1332.v1

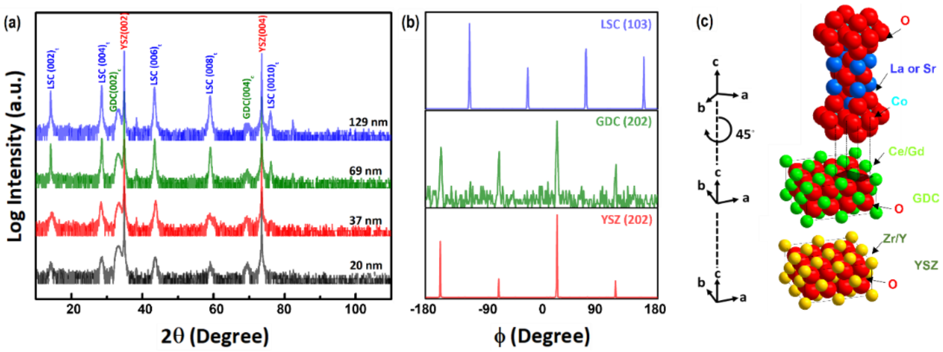

Figure 1. High-resolution X-ray diffraction (Cu K$_\alpha$) analysis. (a) Normal XRD of the $(001)_{\text{tetragonal}}$-oriented epitaxial LSC214 thin films (20, 37, 69, and 129 nm), (b) off-normal XRD of the $(001)_{\text{tetragonal}}$-oriented epitaxial LSC214 thin films (37 nm), GDC and YSZ, and (c) schematic of the crystallographic rotational relationships among the LSC214 $(002)_{\text{tetragonal}}$, GDC $(002)_{\text{cubic}}$, and YSZ $(002)_{\text{cubic}}$.

Table 1. Summary of calculated experimental and relaxed lattice parameters of epitaxial LSC214 thin films on a YSZ substrate with a GDC as the buffer layer obtained from XRD patterns.

Film Thickness (nm)	a (Å)	c (Å)	â (Å)	ĉ (Å)	a strain (%)	c strain (%)
20	3.832	12.454	3.811	12.515	0.574	-0.492
37	3.828	12.467	3.811	12.516	0.457	-0.392
69	3.813	12.491	3.808	12.505	0.134	-0.115
129	3.806	12.506	3.807	12.503	-0.020	0.017

Figure 2a shows the out-of-plane HRXRD scans for the epitaxial LSC214 films grown on water-soluble sacrificial layers. Similar to the epitaxial LSC214 films directly grown on YSZ, only $(00l)_{\text{tetragonal}}$ peaks of LSC214 (where *l* is even) were observed together with $(00l)_{\text{cubic}}$ peaks of GDC, S_1C_2AO or S_2C_1AO, and STO, confirming *c*-axis-oriented LSC214 films with a crystallographic relationship of $(002)_{\text{tetragonal}}$ LSC214 // $(002)_{\text{cubic}}$ GDC // $(008)_{\text{cubic}}$ S_1C_2AO or S_2C_1AO // $(002)_{\text{cubic}}$ STO. Figure 2b schematically illustrates the wet etching process used to fabricate freestanding LSC214 membranes. The cubic GDC buffer (5.451 Å) rotated by 45° provides an effective in-plane spacing ($\frac{\sqrt{2}}{2}$ a_{GDC} = 3.86 Å), which closely matches the in-plane lattice of the S_1C_2AO sacrificial layer (3.851 Å). This near-zero misfit minimizes stored elastic energy. Accordingly, upon dissolving S_1C_2AO, strain relaxation or buckling did not occur, and the released LSC214/GDC bilayer remained flat and defect-free (Figure 2c). In contrast, at the GDC/S_2C_1AO interface, the lattice mismatch is ~1.8% even after the 45° in-plane rotation. When the sacrificial layer was removed and substrate clamping was lost, the accumulated misfit strain relaxed, and therefore the bilayer lowered its elastic energy by developing out-of-plane wrinkles (Figure 2d). The resulting localized deformation effectively relieves residual strain stemming from growth and transfer in the freestanding LSC214/GDC membrane [41].

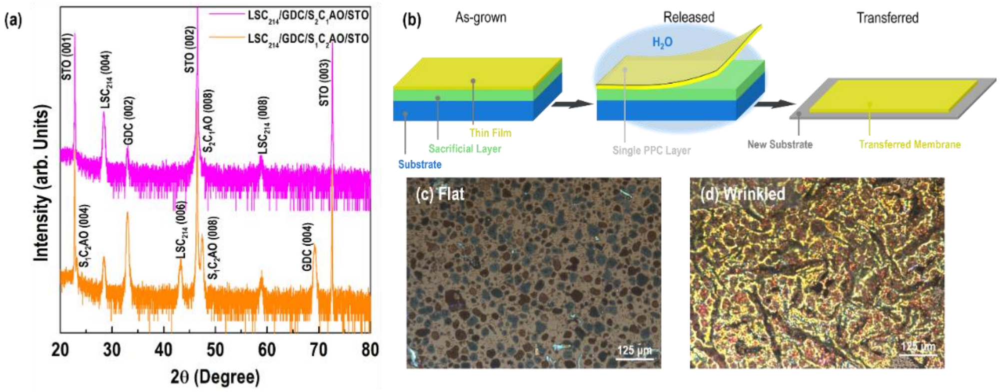

Figure 2. (a) Normal XRD of the $(001)_{tetragonal}$-oriented epitaxial LSC214 thin films on GDC and water-soluble sacrificial layers. (b) schematic of the wet etching method used in this study, showing epitaxial layers after deposition with PLD, during dissolution of sacrificial layer in water, and after transfer onto a new substrate. Optical microscopy images of the surface of (c) flat and (d) wrinkled LSC214 membranes after transfer.

3.2. Electrochemical Properties of the Epitaxial LSC214 Thin Films and Freestanding Membranes

Figure 3a shows representative Nyquist plots for the 20-nm-thick LSC214 film at 550 °C as a function of pO_2. Based on the pO_2 dependence of the three features in the equivalent circuit, each frequency range was determined [60–63]. The high-frequency feature did not change with pO_2, and its magnitude and activation energy (~1.15 eV) matched previously reported values for oxygen ion conduction in YSZ [63]. The mid-frequency feature was independent of pO_2 and is attributed to oxygen ion transport at the LSC214/GDC interface. Its capacitance was also much smaller (~10^{-6} F) than that of the low-frequency feature (~10^{-3} F). In thin film electrodes, the capacitance mainly reflects changes in oxygen content. Accordingly, the low-frequency feature corresponds to oxygen surface reaction. R_{ORR} was taken from the corresponding low frequency element in the equivalent circuit fit. The strong pO_2 dependence of this feature indicates that oxygen surface exchange kinetics governs the ORR in the LSC214 films. Furthermore, the dominant role of surface exchange is further supported by the fact that all film thicknesses are much smaller than the critical thickness for bulk transport limitation (estimated to ~5000 μm for the bulk La_2CoO_4 [27]).

Figure 3b compares impedance spectra at 550 °C and pO_2 = 1 atm for the LSC214 thin films of different thicknesses (20, 37, 69, and 129 nm) and for freestanding membranes (flat and wrinkled, both ~120 nm). The thickest, largely relaxed film (129 nm) was found to exhibit the largest low-frequency semicircle, whereas the thinnest, most tensile-strained film (20 nm) showed the smallest low-frequency semicircle. As thickness increased and epitaxial strain relaxed, the low-frequency semicircle increased systematically. For freestanding membranes of identical thickness (≈120 nm), morphology was decisive. The flat membrane showed a low-frequency semicircle comparable to the relaxed 129-nm epitaxial film, whereas the wrinkled membrane exhibited a substantially smaller low-frequency semicircle comparable to the strained 20-nm film.

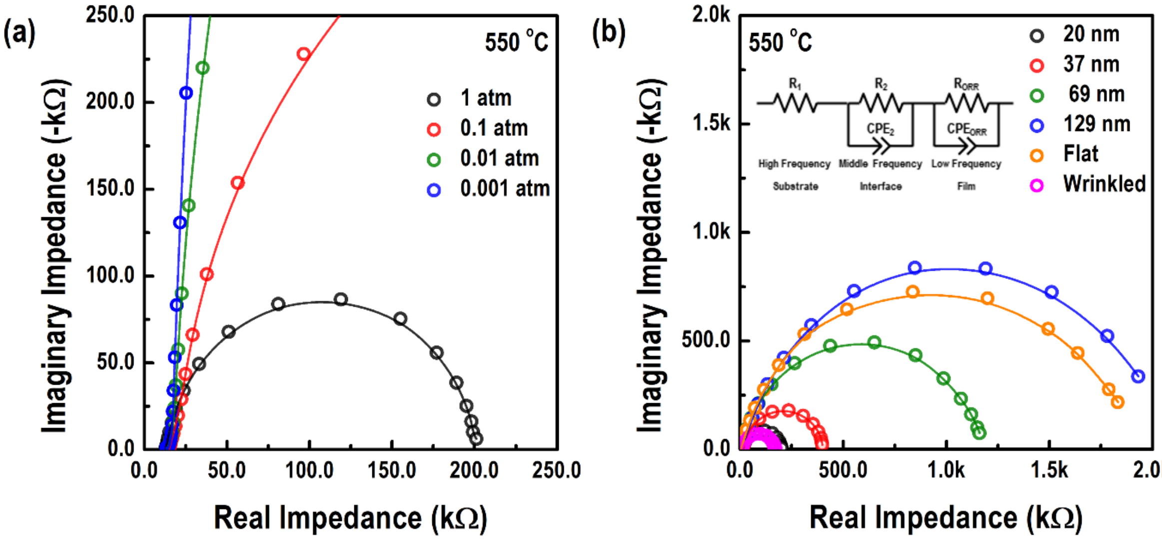

Figure 3. Impedance spectra of microelectrode LSC214 thin films at 550 °C. (a) Nyquist plot of the LSC214 thin film with 20 nm thickness as a function of pO_2. (b) Nyquist plots of the LSC214 thin films with different thicknesses (20, 37, 69, and 129 nm) and freestanding membranes (flat and wrinkled) measured at pO_2 = 1 atm. Inset in (b) shows the equivalent circuit (R_1 = YSZ electrolyte resistance, R_2 = electrode/electrolyte interface resistance, R_{ORR} = ORR resistance, CPE = constant phase element) used to extract ORR kinetics.

doi:10.20944/preprints202512.1332.v1

To investigate the ORR activity of the LSC214 thin films and freestanding membranes, we extracted the k^q and *VSC* from the EIS data (Figure 4). Figure 4a shows the temperature dependence of k^q at 1 atm for the LSC214 films of different thicknesses and for flat and wrinkled membranes. Introducing in-plane tensile strain increased the k^q values of the LSC214 thin films more than one order of magnitude. In contrast, the wrinkled membrane induced by strain relaxation significantly enhanced the k^q values of LSC214 compared to the thin films, whereas the flat membrane exhibited comparable k^q values to the film with the equivalent thickness (~120 nm). It is worth noting that the wrinkled membrane exhibited a higher k^q value compared to the most strained thin film. In addition, the activation energy for oxygen surface exchange of the films was measured at 1 atm, resulting in values of 1.59, 1.52, 1.20, and 1.10 eV for films with thicknesses of 20, 37, 69, and 129 nm, respectively. The pO_2 dependence of k^q ($k^q \propto P_{O_2}^m$) was found to have an exponent m = ~0.65 for the representative 20 nm film (Figure 3a), indicating that the reaction rate-limiting step is a molecular oxygen dissociative adsorption process rather than a charge-transfer process [64,65].

Figure 4b shows *VSC* as a function of temperature for the LSC214 thin films of different thicknesses and freestanding membranes obtained from the EIS data. *VSC* increased systematically as the film thickness decreased (i.e., tensile strain increased), indicating a higher density of redox-active defects and charge carriers in the strained films. Since *VSC* in mixed-conducting cobaltites scales with the concentration of oxygen vacancies and electronic carriers, these trends suggest that tensile strain promotes oxygen vacancy formation in LSC214. Under oxygen-deficient conditions, oxygen transport in $La_{2-x}Sr_xCoO_{4\pm\delta}$ is known to proceed predominantly via oxygen vacancies in the perovskite layers, that is, through vacancy-assisted diffusion [66,67]. These prior results, together with our observed increase in VSC with strain, support our hypothesis that tensile strain in LSC214 enhances the concentration and/or mobility of oxygen vacancies. Combined with our k^q values, these trends are consistent with a vacancy-assisted oxygen reduction mechanism [68] in which adsorbed oxygen species are incorporated into the lattice via oxygen vacancies at the LSC214 surface.

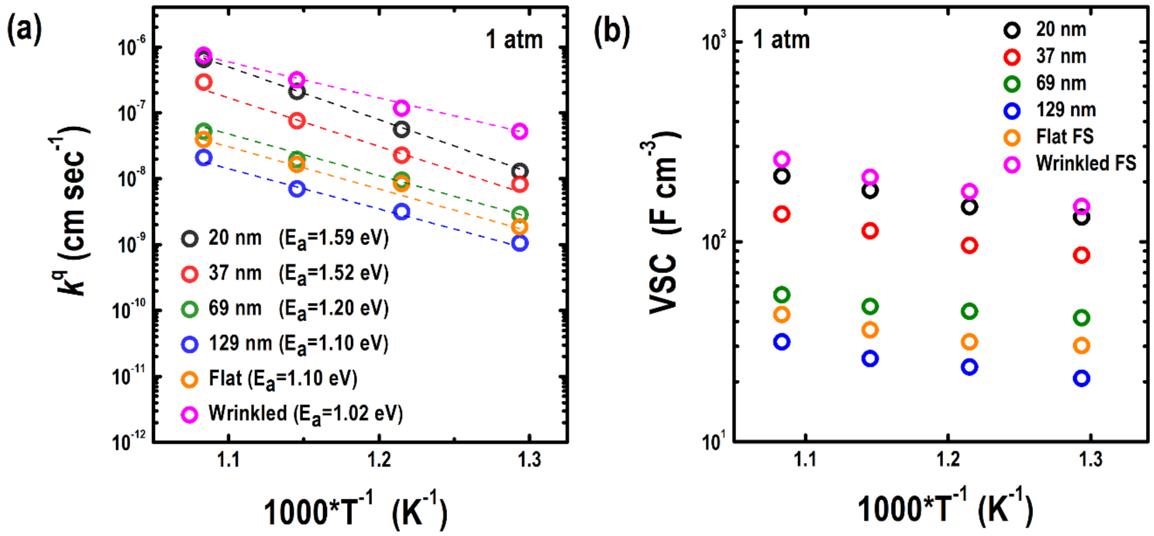

Figure 4. Temperature dependence of (a) the surface exchange coefficient, k^q, and (b) the volume-specific capacitance (VSC) for epitaxial LSC214 thin films with thicknesses of 20, 37, 69, and 129 nm and freestanding membranes calculated from EIS spectra collected at pO_2 = 1 atm.

3.3. Surface Chemistry of the Epitaxial LSC214 Thin Films

To assess thickness-dependent surface chemistry of the LSC214 thin films, area mode Auger electron spectroscopy (AES) was performed on the 37 and 69-nm-thick LSC214 films under three different conditions: pristine, annealed at 1 atm, and annealed at 10^{-3} atm, all at 550 °C for 6 hours (Figure 5). For both thicknesses, Co and Sr spectral features overlapped across all conditions, indicating negligible changes in cation surface composition upon annealing. Relative ratios extracted from AES (Figures 5e and 5f) showed low Co/(La+Sr) consistent with an A-site terminated RP surface (SrO termination) [25] and no systematic variation of Sr/(La+Sr) with thickness or annealing atmosphere. These results suggest that, within the sensitivity and depth of resolution of AES, the surface cation stoichiometry is effectively invariant across thicknesses and annealing conditions. Consequently, the absence of measurable thickness-dependent surface chemistry implies that the observed trends in k_q and m are governed primarily by strain-controlled defect thermodynamics (oxygen-vacancy population) rather than by changes in surface cation composition.

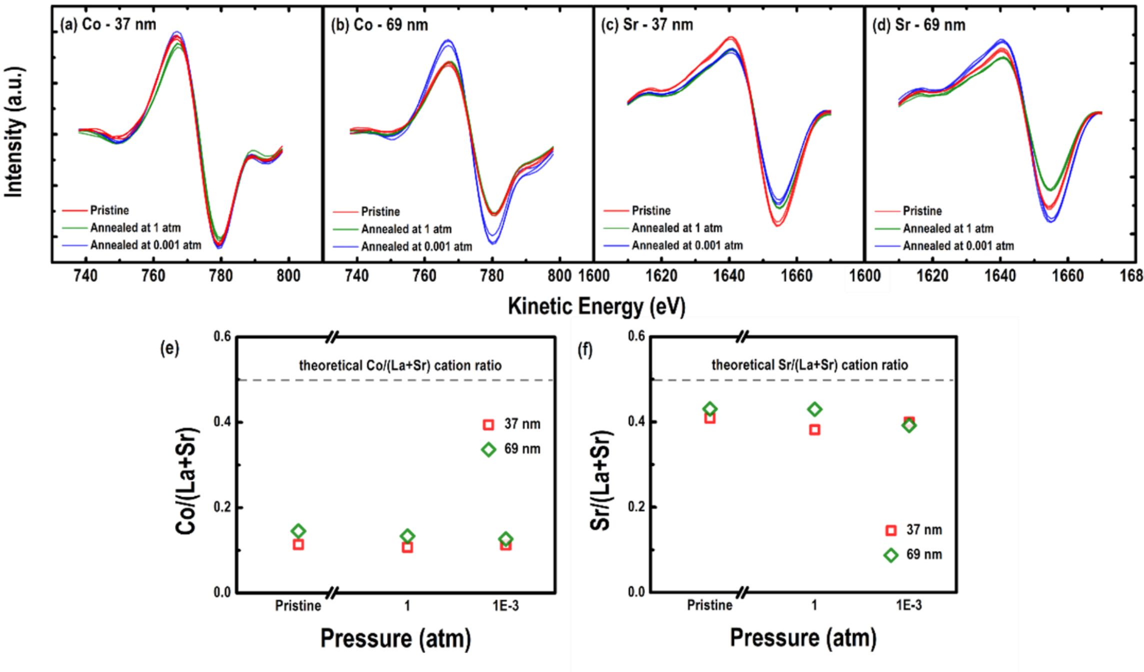

Figure 5. Auger electron spectroscopy (AES) data in area mode for pristine (red) LSC214 thin films and films annealed one at 550 °C at $pO_2 = 1$ atm (green) and $pO_2 = 0.001$ atm (blue). Co cation variation is shown for (a) 37-nm-thick and (b) 69-nm-thick films. Sr cation variation is depicted for (c) 37-nm-thick and (d) 69-nm-thick film. (e) Cation ratios of Co/(La+Sr) and (f) Sr/(La+Sr) extracted from AES of the LSC214 thin films with different annealing conditions.

4. Discussion

As shown in Figure 4, thinner (more tensile-strained) LSC214 films showed larger k_q values, whereas thicker, more relaxed films exhibited smaller k_q values. This trend is consistent with tensile strain lowering the formation energy of oxygen vacancies and shifting the defect equilibrium toward higher vacancy concentrations [22,33,34]. The resulting increase in available carriers and surface defect sites raises the pre-exponential factor for oxygen surface exchange, thereby reducing the ORR polarization resistance. In addition, strained films were found to have higher k_q and higher E_a than relaxed films.

For RP oxides, the bulk oxygen 2p band center has emerged as a useful descriptor that correlates with both oxygen surface exchange rates and activation barriers. Across oxygen-excess RP oxides, a lower oxygen 2p level aligns with higher surface exchange rates and lower barriers, whereas ABO_3 perovskites show the opposite trend [59]. In vacancy dominated RP oxides such as LSC214, the behavior is more consistent with ABO_3 perovskites, where an upward shift of the oxygen 2p level that stabilizes vacancies is associated with enhanced surface exchange. In RP oxides, oxygen defect formation energies vary approximately linearly with the oxygen 2p band center, and shifting the oxygen 2p level upward stabilizes vacancies by lowering their formation energy while destabilizing interstitials [67]. A strain driven upshift of the oxygen 2p band center, accompanied by enhanced oxygen surface exchange kinetics and increased oxygen vacancy concentration, has been demonstrated in tensile strained $La_{0.6}Sr_{0.4}CoO_{3-\delta}$ epitaxial films on YSZ [33]. In our films, tensile strain plausibly perturbs the electronic structure in this RP-like direction, producing exactly the combination we observe, more exchange active sites (faster k^q) together with a modest increase in the E_a.

For the freestanding LSC214 membranes, the flat membrane behaves similarly to the relaxed epitaxial film (comparable polarization resistance and $E_a \approx 1.10$ eV). The wrinkled membrane showed a markedly smaller ORR arc, higher k^q, and a slightly lower E_a (≈ 1.01 eV). Because thickness and composition were fixed, two morphology specific factors were the likely causes: (i) effective area amplification, which increases the number of accessible exchange sites per projected footprint, and (ii) local variations in strain and curvature across the wrinkles, which can favor adsorption and adjust near-surface vacancy equilibria. The small decrease in E_a is consistent with these geometric and local-strain advantages.

Taken together, these findings establish epitaxial strain and membrane wrinkling as practical, orthogonal levers for tuning ORR in RP oxides. For device relevant platforms (films on YSZ), thickness-controlled strain is a robust route to enhance k^q. For flexible or transfer architectures, controlled wrinkling further boosts activity while modestly lowering E_a. Future work that quantifies the wrinkle-induced roughness factor and correlates it with k^q and E_a would help separate geometric from electronic contributions and refine predictive design rules.

5. Conclusions

In summary, this study demonstrates that the ORR activity of LSC214 thin films is strongly influenced by epitaxial strain and wrinkle formation. Compared to relaxed films, tensile-strained LSC214 exhibited higher k^q values, reflecting enhanced ORR kinetics, but also showed increased activation energy. This behavior is consistent with an increase in oxygen vacancy concentration and/or mobility under in-plane tensile strain. Wrinkle formation in freestanding LSC membranes further enhanced ORR activity, increasing the k^q value while lowering the activation energy due to a larger active surface area generated upon strain relaxation. *VSC* analysis further supports the correlation between oxygen vacancy concentration and the improved ORR performance in both strained films and wrinkled membranes. AES measurements indicate that the surface cation stoichiometry remains effectively invariant across thicknesses and annealing conditions. These findings highlight the pivotal role of epitaxial strain in modulating oxygen surface exchange and emphasize the necessity of integrating surface chemical analysis with electrochemical metrics to design highly active oxide catalysts for energy conversion applications.

Author Contributions: Conceptualization, D.L. and H.R.; formal analysis, H.R.; Investigation, H.R., E.S.; data curation, H.R., E.S.; writing—original draft preparation, H.R.; writing—review and editing, D.L., M.E.; supervision and project administration, D.L. All authors have read and agreed to the published version of the manuscript.

Funding: This research was funded by the National Science Foundation under NSF Award Number DMR-2340234.

Acknowledgments: Sample synthesis and structural characterization were conducted at the Center for Nanophase Materials Sciences (CNMS), which is a U.S. Department of Energy, Office of Science User Facility at Oak Ridge National Laboratory.

Conflicts of Interest: The authors declare no conflicts of interest.

References

1. Sahini, M.G.; Mwankemwa, B.S.; Kanas, N. BaxSr1-xCoyFe1-yO3-δ (BSCF) mixed ionic-electronic conducting (MIEC) materials for oxygen separation membrane and SOFC applications: insights into processing, stability, and functional properties. *Ceramics International* **2022**, *48*, 2948-2964.

doi:10.20944/preprints202512.1332.v1

2. Zhang, K.; Ge, L.; Ran, R.; Shao, Z.; Liu, S. Synthesis, characterization and evaluation of cation-ordered LnBaCo2O5+ δ as materials of oxygen permeation membranes and cathodes of SOFCs. *Acta Materialia* **2008**, *56*, 4876-4889.
3. Adler, S.B. Chemical expansivity of electrochemical ceramics. *Journal of the American Ceramic Society* **2001**, *84*, 2117-2119.
4. Mutoro, E.; Crumlin, E.J.; Biegalski, M.D.; Christen, H.M.; Shao-Horn, Y. Enhanced oxygen reduction activity on surface-decorated perovskite thin films for solid oxide fuel cells. *Energy & Environmental Science* **2011**, *4*, 3689-3696.
5. Yang, Q.; Wang, G.; Wu, H.; Beshiwork, B.A.; Tian, D.; Zhu, S.; Yang, Y.; Lu, X.; Ding, Y.; Ling, Y. A high-entropy perovskite cathode for solid oxide fuel cells. *Journal of Alloys and Compounds* **2021**, *872*, 159633.
6. Kim, J.H.; Kim, D.; Ahn, S.; Kim, K.J.; Jeon, S.; Lim, D.-K.; Kim, J.K.; Kim, U.; Im, H.-N.; Koo, B. An universal oxygen electrode for reversible solid oxide electrochemical cells at reduced temperatures. *Energy & Environmental Science* **2023**, *16*, 3803-3814.
7. Bai, J.; Zhou, D.; Zhu, X.; Wang, N.; Liang, Q.; Chen, R.; Lu, H.; Li, J.; Yan, W. Bi0. 5Sr0. 5FeO3-δ perovskite B-site doped Ln (Nd, Sm) as cathode for high performance Co-free intermediate temperature solid oxide fuel cell. *Ceramics International* **2023**, *49*, 28682-28692.
8. Yang, G.; Jung, W.; Ahn, S.-J.; Lee, D. Controlling the oxygen electrocatalysis on perovskite and layered oxide thin films for solid oxide fuel cell cathodes. *Applied Sciences* **2019**, *9*, 1030.
9. Crumlin, E.J.; Ahn, S.-J.; Lee, D.; Mutoro, E.; Biegalski, M.D.; Christen, H.M.; Shao-Horn, Y. Oxygen electrocatalysis on epitaxial La0. 6Sr0. 4CoO3-δ perovskite thin films for solid oxide fuel cells. *Journal of the Electrochemical Society* **2012**, *159*, F219.
10. Crumlin, E.J.; Mutoro, E.; Liu, Z.; Grass, M.E.; Biegalski, M.D.; Lee, Y.-L.; Morgan, D.; Christen, H.M.; Bluhm, H.; Shao-Horn, Y. Surface strontium enrichment on highly active perovskites for oxygen electrocatalysis in solid oxide fuel cells. *Energy & Environmental Science* **2012**, *5*, 6081-6088.
11. Safian, S.D.; Abd Malek, N.I.; Jamil, Z.; Lee, S.W.; Tseng, C.J.; Osman, N. Study on the surface segregation of mixed ionic-electronic conductor lanthanum-based perovskite oxide La1− xSrxCo1− yFeyO3− δ materials. *International Journal of Energy Research* **2022**, *46*, 7101-7117.
12. Wei, M.; Li, H.; Chen, X.; Guo, G.; Liu, Y.; Zhang, D. First-principles study of interfacial effects toward oxygen reduction reaction of palladium/La1-xSrxCo1-yFeyO3-δ cathodes in solid oxide fuel cells. *Applied Surface Science* **2021**, *562*, 150218.
13. Adler, S.B. Mechanism and kinetics of oxygen reduction on porous La1− xSrxCoO3− δ electrodes. *Solid State Ionics* **1998**, *111*, 125-134.
14. Tyunina, M.; Pacherova, O.; Kocourek, T.; Dejneka, A. Anisotropic chemical expansion due to oxygen vacancies in perovskite films. *Scientific Reports* **2021**, *11*, 15247.
15. Li, Z.; Peng, M.; Zhao, Y.; Li, J.; Sun, Y. Minimized thermal expansion mismatch of cobalt-based perovskite air electrodes for solid oxide cells. *Nanoscale* **2021**, *13*, 20299-20308.
16. Rupp, G.M.; Limbeck, A.; Kubicek, M.; Penn, A.; Stöger-Pollach, M.; Friedbacher, G.; Fleig, J. Correlating surface cation composition and thin film microstructure with the electrochemical performance of lanthanum strontium cobaltite (LSC) electrodes. *Journal of Materials Chemistry A* **2014**, *2*, 7099-7108.
17. Wen, Y.; Yang, T.; Lee, D.; Lee, H.N.; Crumlin, E.J.; Huang, K. Temporal and thermal evolutions of surface Sr-segregation in pristine and atomic layer deposition modified La 0.6 Sr 0.4 CoO 3− δ epitaxial films. *Journal of Materials Chemistry A* **2018**, *6*, 24378-24388.
18. Koo, B.; Kim, K.; Kim, J.K.; Kwon, H.; Han, J.W.; Jung, W. Sr segregation in perovskite oxides: why it happens and how it exists. *Joule* **2018**, *2*, 1476-1499.
19. Lee, D.; Grimaud, A.; Crumlin, E.J.; Mezghani, K.; Habib, M.A.; Feng, Z.; Hong, W.T.; Biegalski, M.D.; Christen, H.M.; Shao-Horn, Y. Strain influence on the oxygen electrocatalysis of the (100)-oriented epitaxial La2NiO4+ δ thin films at elevated temperatures. *The Journal of Physical Chemistry C* **2013**, *117*, 18789-18795.
20. Lee, D.; Lee, Y.-L.; Grimaud, A.; Hong, W.T.; Biegalski, M.D.; Morgan, D.; Shao-Horn, Y. Strontium influence on the oxygen electrocatalysis of La 2− x Sr x NiO 4±δ (0.0≤ x Sr≤ 1.0) thin films. *Journal of Materials Chemistry A* **2014**, *2*, 6480-6487.

21. Burriel, M.; Garcia, G.; Santiso, J.; Kilner, J.A.; Chater, R.J.; Skinner, S.J. Anisotropic oxygen diffusion properties in epitaxial thin films of La 2 NiO 4+ δ. *Journal of materials chemistry* **2008**, *18*, 416-422.
22. Yang, G.; El Loubani, M.; Hill, D.; Keum, J.K.; Lee, D. Control of crystallographic orientation in Ruddlesden-Popper for fast oxygen reduction. *Catalysis Today* **2023**, *409*, 87-93.
23. Ma, T.; Xia, T.; Li, Q.; Sun, L.; Huo, L.; Zhao, H. Highly electrocatalytic activity Ruddlesden− Popper type electrode materials for solid oxide fuel cells. *Journal of the European Ceramic Society* **2022**, *42*, 490-498.
24. Lee, D.; Lee, H.N. Controlling oxygen mobility in Ruddlesden–Popper oxides. *Materials* **2017**, *10*, 368.
25. Chen, Y.; Téllez, H.; Burriel, M.n.; Yang, F.; Tsvetkov, N.; Cai, Z.; McComb, D.W.; Kilner, J.A.; Yildiz, B. Segregated chemistry and structure on (001) and (100) surfaces of (La1−x Sr x) 2CoO4 override the crystal anisotropy in oxygen exchange kinetics. *Chemistry of Materials* **2015**, *27*, 5436-5450.
26. Boehm, E.; Bassat, J.-M.; Steil, M.; Dordor, P.; Mauvy, F.; Grenier, J.-C. Oxygen transport properties of La2Ni1− xCuxO4+ δ mixed conducting oxides. *Solid State Sciences* **2003**, *5*, 973-981.
27. Munnings, C.; Skinner, S.; Amow, G.; Whitfield, P.; Davidson, I. Oxygen transport in the La2Ni1− xCoxO4+ δ system. *Solid State Ionics* **2005**, *176*, 1895-1901.
28. Brown, I.; Altermatt, D. Bond-valence parameters obtained from a systematic analysis of the inorganic crystal structure database. *Acta Crystallographica Section B: Structural Science* **1985**, *41*, 244-247.
29. Nitadori, T.; Muramatsu, M.; Misono, M. Valence control, reactivity of oxygen, and catalytic activity of lanthanum strontium cobalt oxide (La2-xSrxCoO4). *Chemistry of Materials* **1989**, *1*, 215-220.
30. Zhao, C.; Liu, X.; Zhang, W.; Zheng, Y.; Li, Y.; Yu, B.; Wang, J.; Chen, J. Measurement of oxygen reduction/evolution kinetics enhanced (La, Sr) CoO3/(La, Sr) 2CoO4 hetero-structure oxygen electrode in operating temperature for SOCs. *International Journal of Hydrogen Energy* **2019**, *44*, 19102-19112.
31. Lee, D.; Lee, Y.-L.; Hong, W.T.; Biegalski, M.D.; Morgan, D.; Shao-Horn, Y. Oxygen surface exchange kinetics and stability of (La, Sr) 2 CoO 4±δ/La 1− x Sr x MO 3− δ (M= Co and Fe) hetero-interfaces at intermediate temperatures. *Journal of Materials Chemistry A* **2015**, *3*, 2144-2157.
32. Fleig, J.; Baumann, F.; Brichzin, V.; Kim, H.R.; Jamnik, J.; Cristiani, G.; Habermeier, H.U.; Maier, J. Thin film microelectrodes in SOFC electrode research. *Fuel Cells* **2006**, *6*, 284-292.
33. Lee, D.; Jacobs, R.; Jee, Y.; Seo, A.; Sohn, C.; Ievlev, A.V.; Ovchinnikova, O.S.; Huang, K.; Morgan, D.; Lee, H.N. Stretching epitaxial La0. 6Sr0. 4CoO3− δ for fast oxygen reduction. *The Journal of Physical Chemistry C* **2017**, *121*, 25651-25658.
34. Yang, G.; El Loubani, M.; Handrick, D.; Stevenson, C.; Lee, D. Understanding the influence of strain-modified oxygen vacancies and surface chemistry on the oxygen reduction reaction of epitaxial La0. 8Sr0. 2CoO3-δ thin films. *Solid State Ionics* **2023**, *393*, 116171.
35. Yang, G.; El Loubani, M.; Chalaki, H.R.; Kim, J.; Keum, J.K.; Rouleau, C.M.; Lee, D. Tuning ionic conductivity in fluorite Gd-doped CeO2-Bixbyite RE2O3 (RE= Y and Sm) multilayer thin films by controlling interfacial strain. *ACS Applied Electronic Materials* **2023**, *5*, 4556-4563.
36. Wen, K.; Lv, W.; He, W. Interfacial lattice-strain effects on improving the overall performance of micro-solid oxide fuel cells. *Journal of Materials Chemistry A* **2015**, *3*, 20031-20050.
37. Santiso, J.; Burriel, M. Deposition and characterisation of epitaxial oxide thin films for SOFCs. *Journal of Solid State Electrochemistry* **2011**, *15*, 985-1006.
38. Bassat, J.-M.; Burriel, M.; Wahyudi, O.; Castaing, R.m.; Ceretti, M.; Veber, P.; Weill, I.; Villesuzanne, A.; Grenier, J.-C.; Paulus, W. Anisotropic oxygen diffusion properties in Pr2NiO4+ δ and Nd2NiO4+ δ single crystals. *The Journal of Physical Chemistry C* **2013**, *117*, 26466-26472.
39. Burriel, M.; Téllez, H.; Chater, R.J.; Castaing, R.; Veber, P.; Zaghrioui, M.; Ishihara, T.; Kilner, J.A.; Bassat, J.-M. Influence of crystal orientation and annealing on the oxygen diffusion and surface exchange of La2NiO4+ δ. *The Journal of Physical Chemistry C* **2016**, *120*, 17927-17938.
40. Tsvetkov, N.; Lu, Q.; Chen, Y.; Yildiz, B. Accelerated oxygen exchange kinetics on Nd2NiO4+ δ thin films with tensile strain along c-axis. *ACS nano* **2015**, *9*, 1613-1621.
41. Yun, S.; le Cozannet, T.E.; Christoffersen, C.H.; Brand, E.; Jespersen, T.S.; Pryds, N. Strain engineering: perfecting freestanding perovskite oxide fabrication. *Small* **2024**, *20*, 2310782.

42. Lu, Q.; Liu, Z.; Yang, Q.; Cao, H.; Balakrishnan, P.; Wang, Q.; Cheng, L.; Lu, Y.; Zuo, J.-M.; Zhou, H. Engineering magnetic anisotropy and emergent multidirectional soft ferromagnetism in ultrathin freestanding LaMnO3 films. *ACS nano* **2022**, *16*, 7580-7588.
43. Li, Y.; Xiang, C.; Chiabrera, F.M.; Yun, S.; Zhang, H.; Kelly, D.J.; Dahm, R.T.; Kirchert, C.K.; Cozannet, T.E.L.; Trier, F. Stacking and twisting of freestanding complex oxide thin films. *Advanced materials* **2022**, *34*, 2203187.
44. Ji, D.; Cai, S.; Paudel, T.R.; Sun, H.; Zhang, C.; Han, L.; Wei, Y.; Zang, Y.; Gu, M.; Zhang, Y. Freestanding crystalline oxide perovskites down to the monolayer limit. *Nature* **2019**, *570*, 87-90.
45. Varshney, S.; Ramis, M.; Choo, S.; Coll, M.; Jalan, B. Epitaxially grown single-crystalline SrTiO 3 membranes using a solution-processed, amorphous SrCa 2 Al 2 O 6 sacrificial layer. *Journal of Materials Chemistry C* **2024**, *12*, 13809-13815.
46. Dong, G.; Li, S.; Li, T.; Wu, H.; Nan, T.; Wang, X.; Liu, H.; Cheng, Y.; Zhou, Y.; Qu, W. Periodic wrinkle-patterned single-crystalline ferroelectric oxide membranes with enhanced piezoelectricity. *Advanced materials* **2020**, *32*, 2004477.
47. Liu, H.; Yuan, H.; Dong, G.; Wu, K.; Liu, G.; Sun, J.; Zhou, Z.; Liu, M. Tunable friction properties of periodic wrinkled BaTiO3 membranes. *Advanced Materials Interfaces* **2022**, *9*, 2102316.
48. Liu, W.; Wang, H. Flexible oxide epitaxial thin films for wearable electronics: Fabrication, physical properties, and applications. *Journal of Materiomics* **2020**, *6*, 385-396.
49. la O, G.J.; Ahn, S.J.; Crumlin, E.; Orikasa, Y.; Biegalski, M.D.; Christen, H.M.; Shao-Horn, Y. Catalytic activity enhancement for oxygen reduction on epitaxial perovskite thin films for solid-oxide fuel cells. *Angewandte Chemie (International ed. in English)* **2010**, *49*.
50. Mitterdorfer, A.; Gauckler, L. La2Zr2O7 formation and oxygen reduction kinetics of the La0. 85Sr0. 15MnyO3, O2 (g)| YSZ system. *Solid State Ionics* **1998**, *111*, 185-218.
51. Yashima, M.; Sasaki, S.; Kakihana, M.; Yamaguchi, Y.; Arashi, H.; Yoshimura, M. Oxygen-induced structural change of the tetragonal phase around the tetragonal–cubic phase boundary in ZrO2–YO1. 5 solid solutions. *Structural Science* **1994**, *50*, 663-672.
52. James, M.; Tedesco, A.; Cassidy, D.; Colella, M.; Smythe, P. The phase diagram and crystal chemistry of strontium-doped rare earth cobaltates: Ln2− xSrxCoO4+ δ (Ln= La–Dy). *Journal of alloys and compounds* **2006**, *419*, 201-207.
53. Christen, H.M.; Specht, E.D.; Silliman, S.S.; Harshavardhan, K. Ferroelectric and antiferroelectric coupling in superlattices of paraelectric perovskites at room temperature. *Physical Review B* **2003**, *68*, 020101.
54. Noh, D.; Hwu, Y.; Je, J.; Hong, M.; Mannaerts, J. Strain relaxation in Fe3 (Al, Si)/GaAs: An x-ray scattering study. *Applied physics letters* **1996**, *68*, 1528-1530.
55. Maier, J. On the correlation of macroscopic and microscopic rate constants in solid state chemistry. *Solid State Ionics* **1998**, *112*, 197-228.
56. Fleig, J.; Maier, J. The polarization of mixed conducting SOFC cathodes: Effects of surface reaction coefficient, ionic conductivity and geometry. *Journal of the European Ceramic Society* **2004**, *24*, 1343-1347.
57. Maier, J. Physical chemistry of ionic materials: ions and electrons in solids; John Wiley & Sons: 2023.
58. Vashook, V.; Ullmann, H.; Olshevskaya, O.; Kulik, V.; Lukashevich, V.; Kokhanovskij, L. Composition and electrical conductivity of some cobaltates of the type La2− xSrxCoO4. 5− x/2±δ. *Solid State Ionics* **2000**, *138*, 99-104.
59. Lee, Y.-L.; Lee, D.; Wang, X.R.; Lee, H.N.; Morgan, D.; Shao-Horn, Y. Kinetics of oxygen surface exchange on epitaxial Ruddlesden–Popper phases and correlations to first-principles descriptors. *The Journal of Physical Chemistry Letters* **2016**, *7*, 244-249.
60. Adler, S.B. Factors governing oxygen reduction in solid oxide fuel cell cathodes. *Chemical reviews* **2004**, *104*, 4791-4844.
61. Adler, S.B.; Lane, J.A.; Steele, B.C. Electrode kinetics of porous mixed-conducting oxygen electrodes. *Journal of the electrochemical society* **1996**, *143*, 3554.
62. Kawada, T.; Suzuki, J.; Sase, M.; Kaimai, A.; Yashiro, K.; Nigara, Y.; Mizusaki, J.; Kawamura, K.; Yugami, H. Determination of oxygen vacancy concentration in a thin film of La0. 6Sr0. 4CoO3− δ by an electrochemical method. *Journal of the Electrochemical Society* **2002**, *149*, E252.

doi:10.20944/preprints202512.1332.v1

63. Yang, Y.; Chen, C.; Chen, S.; Chu, C.; Jacobson, A. Impedance studies of oxygen exchange on dense thin film electrodes of La0. 5Sr0. 5CoO3− δ. *Journal of the Electrochemical Society* **2000**, *147*, 4001.
64. Takeda, Y.; Kanno, R.; Noda, M.; Tomida, Y.; Yamamoto, O. Cathodic polarization phenomena of perovskite oxide electrodes with stabilized zirconia. *Journal of the Electrochemical Society* **1987**, *134*, 2656.
65. Escudero, M.; Aguadero, A.; Alonso, J.A.; Daza, L. A kinetic study of oxygen reduction reaction on La2NiO4 cathodes by means of impedance spectroscopy. *Journal of Electroanalytical Chemistry* **2007**, *611*, 107-116.
66. Tealdi, C.; Ferrara, C.; Mustarelli, P.; Islam, M.S. Vacancy and interstitial oxide ion migration in heavily doped La 2− x Sr x CoO 4±δ. *Journal of Materials Chemistry* **2012**, *22*, 8969-8975.
67. Xie, W.; Lee, Y.-L.; Shao-Horn, Y.; Morgan, D. Oxygen Point Defect Chemistry in Ruddlesden–Popper Oxides (La1–x Sr x) 2MO4±δ (M= Co, Ni, Cu). *The journal of physical chemistry letters* **2016**, *7*, 1939-1944.
68. Miyoshi, S.; Takeshita, A.; Okada, S.; Yamaguchi, S. Rate-determining elementary step of oxygen reduction reaction at (La, Sr) CoO3-based cathode surface. *Solid State Ionics* **2016**, *285*, 202-208.